Original Article

Reflections on the Spatial Performance of Atom Probe Tomography in the Analysis of Atomic Neighborhoods

Baptiste Gault[1,2]* , Benjamin Klaes[3] , Felipe F. Morgado[1], Christoph Freysoldt[1] , Yue Li[1], Frederic De Geuser[4], Leigh T. Stephenson[1] and François Vurpillot[3]

[1]Max-Planck-Institut für Eisenforschung, Max-Planck-Str. 1, Düsseldorf 40237, Germany; [2]Department of Materials, Royal School of Mines, Imperial College, Prince Consort Road, London SW7 2BP, UK; [3]Groupe Physique des Matériaux, Université de Rouen, Saint Etienne du Rouvray, Normandie 76800, France and [4]Université Grenoble Alpes, CNRS, Grenoble INP, SIMAP, Grenoble 38000, France

Abstract

Atom probe tomography (APT) is often introduced as providing "atomic-scale" mapping of the composition of materials and as such is often exploited to analyze atomic neighborhoods within a material. Yet quantifying the actual spatial performance of the technique in a general case remains challenging, as it depends on the material system being investigated as well as on the specimen's geometry. Here, by using comparisons with field-ion microscopy experiments, field-ion imaging and field evaporation simulations, we provide the basis for a critical reflection on the spatial performance of APT in the analysis of pure metals, low alloyed systems and concentrated solid solutions (i.e., akin to high-entropy alloys). The spatial resolution imposes strong limitations on the possible interpretation of measured atomic neighborhoods, and directional neighborhood analyses restricted to the depth are expected to be more robust. We hope this work gets the community to reflect on its practices, in the same way, it got us to reflect on our work.

Key words: compositionally complex alloys, field evaporation, image simulations, nearest neighbors

(Received 2 March 2021; revised 11 September 2021; accepted 1 October 2021)

Introduction

Atom probe tomography (APT) stems from the field-ion microscopy (FIM) that allowed Erwin Müller and his collaborators to image individual atoms already in the 1950s (Müller & Bahadur, 1956). In FIM, the image of each of the surface atoms is formed by the successive impact of thousands of gas ions per second on the screen. The ion trajectories in FIM are expected to be determined, for a given specimen geometry and microscope, only by the distribution of the electrostatic field (Smith & Walls, 1978), assuming that dynamic effects associated with the pulsed voltage can be neglected. To a first approximation, the projection of these ions can be well reproduced by an equidistant projection (Wilkes et al., 1974), or, to a certain extent, by a pseudo-stereographic projection (Blavette et al., 1982; Cerezo et al., 1999; De Geuser & Gault, 2017).

The first design of atom probes involved using FIM to target regions of interest at the specimen's surface and specifically allow certain imaged atoms to pass through a probe hole in the FIM screen to reveal their elemental identity by time-of-flight mass spectrometry. Already then, it became evident that there were so-called aiming errors (Krishnaswamy et al., 1975) that

meant that atoms imaged by FIM would not end up being analyzed as they "missed" the hole. The development of the imaging atom probe (Panitz, 1973), with a field of view comparable to FIM but with a limited analytical range, demonstrated that the imaged position of a surface atom by FIM and the impact position of this same atom following field evaporation were dissimilar.

These differences can be understood as image gas ions forming the field-ion micrograph originate from a region located 1–5 Angstroms above the surface typically near the critical distance for ionization x_c, while as the specimen's atoms ionize and desorb, they do so at the surface. The ions generated by field ionization and field evaporation, hence, do not travel through the same electrostatic field. This is summarized in Figure 1. It is in the early stages of its flight, departing from the surface, that the ion is most subject to aberrations. Indeed, right at the surface, the atomic roughness leads to very strong local variations of the electrostatic field that are well reproduced by finite-element simulations (Vurpillot et al., 2000a). These highly localized gradients can cause very local surface rearrangements by short-range surface migrations (Waugh et al., 1976), and it was proposed that atoms in the process of leaving the surface "roll-up" on their neighbors (Schmidt et al., 1993), and demonstrated this experimentally for Rh (Suchorski et al., 1996). Sanchez et al. (2004) used density-functional theory (DFT) under intense electrostatic fields to study the energy barrier for field evaporation and field-assisted surface diffusion in the case of Al, and showed that they were linked—that is, the magnitude of the electric fields necessary for field

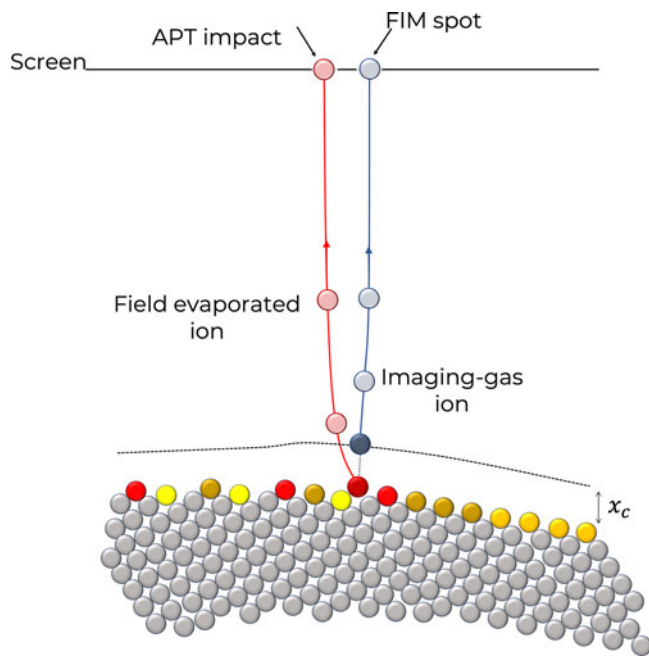*Corresponding author: Baptiste Gault, E-mail: b.gault@mpie.de

Fig. 1. Schematic diagram of the difference between the trajectories of a population of imaging gas ions, in blue, leading to the formation of an individual spot on a field-ion micrograph, and, in red, for an individual field evaporated ion leading to a single detector impact in atom probe tomography.

evaporation also greatly facilitate surface diffusion, facilitating the roll-up. More recently, Ashton et al. (2020) further demonstrated by DFT that the roll-up on neighbors was the energetically favorable path to field evaporation in the case of W. These studies on pure metals with the evaporation field ranging from low (Al) to medium (Rh) to high (W) suggest that the roll-up may be affecting most metals, which agrees with the suggestion of Wada (1984) that above a relatively modest temperature, the DC field evaporation rate is controlled by surface diffusion processes.

Whereas APT's depth resolution is sufficient to resolve interatomic distances across a wide range of families of planes, materials, and experimental conditions (Vurpillot et al., 2001; Cadel et al., 2009; Gault et al., 2010a; Jenkins et al., 2020), these effects combine to limit the lateral resolution of APT generally to more than an interatomic distance based on simulations (Vurpillot et al., 2000b; Vurpillot & Oberdorfer, 2015) and experimentally (Vurpillot et al., 2001; Haley et al., 2009).

These studies were mostly theoretical or on pure metals. Yet APT is nowadays used mostly by materials scientists and engineers interested in mapping the composition of small secondary phase particles or localized compositional fluctuations associated with solute clustering or short-range ordering. Assessing the spatial performance of APT in this context is a true challenge. Recently, De Geuser and Gault performed a systematic review of the literature comparing small-angle scattering to APT and proposed that the spatial resolution in the analysis of nearly spherical particles was limited to somewhere in the range of 0.5–1.5 nm (De Geuser & Gault, 2020). Their study highlighted the complexity to pinpoint an individual value as the resolution will depend on the difference in the field evaporation behavior of the matrix and that of the precipitate. This approach is however not directly transferable to all analyses, in particular localized segregations and compositionally complex solid solutions, that is, high-entropy alloys.

In the analyses of these alloys, it is common to study the statistical distribution of alloying elements in an APT dataset in order to compare it to a random distribution, for instance by binning the data into blocks of a certain number of atoms (Hetherington et al., 1991; Moody et al., 2008). This approach is often referred to as "frequency distribution," and it became commonly used to study compositional fluctuations in spinodally decomposing systems, that is, over length scales in the range of nanometers. Its applicability to solute clustering or short-range ordering, that is, over interatomic distances, has not been assessed. Yet, a cornucopia of articles on bulk metallic glasses (Miller et al., 2003; Kontis et al., 2018; Sarker et al., 2018), nanocrystalline alloys (Detor et al., 2005), high-entropy alloys (Deng et al., 2015; Rao et al., 2017), and other compositionally complex alloys, as well as semiconductors (Galtrey et al., 2007) use it to assess an absence of solute clusters or short-range order.

An alternative method is to directly quantify the distance between nearest neighbors (Shariq et al., 2007; Stephenson et al., 2007) and compare the distribution of distances to the one obtained from a randomly labeled dataset. The latter is a separate, duplicated reconstructed dataset in which the atomic positions are maintained, but the mass-to-charge ratios are swapped randomly, mimicking a randomly distributed set of atoms. The comparison of these two distributions is only typically visual and rarely quantitatively assessed statistically.

Here, we want to offer some reflections and new insights into the spatial performance of APT, based on experimental and computational results, in part based on (in)direct comparison with FIM. The renewed interest in FIM (Vurpillot et al., 2017), including combined with new simulation approaches (Katnagallu et al., 2018, 2019; Klaes et al., 2021), and the development of the analytical FIM (Katnagallu et al., 2019) enable us to provide a critical perspective on the analysis of local neighborhoods by APT in the case of pure metals, local segregations in dilute alloys, and concentrated alloys.

Methods

Ion Trajectory Modeling

Here two sets of simulations are reported, both make use of the field evaporation simulation framework introduced in Rolland et al. (2015). This approach is meshless and uses the Robin model to determine the local charges on each atom at the surface of a field emitter, and then derives the electric field distribution at and in the vicinity of the surface. The simulations of the field evaporation behavior of the NiRe binary alloy and the concentrated alloys were performed using the latest version of this model described in detail in Klaes et al. (2021).

In addition, recently, Klaes et al. (2021) included the possibility to perform field-ion micrograph simulations. This model allows for simulating the trajectories of both the image gas ions departing from the ionization zone above the specimen's surface and the field evaporated ions departing from the surface itself. The details of the simulation technique can be found in Klaes et al. (2021). The set of simulations reported for FIM make use of this model.

Analytical FIM

In Katnagallu et al. (2019), a new approach termed analytical field-ion microscopy (aFIM) was introduced that makes use of

the single-particle detector of a commercial atom probe (the LEAP 5000 XS) and the associated time-of-flight mass spectrometer to perform field-ion microscopy under relatively low imaging gas pressure. Here, pure tungsten needles were prepared from a drawn wire most often exhibiting a $\langle 110 \rangle$ z-axis orientation, by using electrochemical polishing at 5–8 VAC in a 5% molar NaOH solution. Pure He was introduced in the LEAP analysis chamber, following flushing and evacuating the gas mixing chamber twice with pure gas, and refilling it to approximately 1 Torr (with 1 Torr approx. 133 Pa). For FIM, the specimen temperature was set to 50 K and, with a manual leak valve, a low pressure in the range of 1×10^{-7} Torr of He then admitted into the analysis chamber. The LEAP was operated in high-voltage (HV) pulsing mode at a pulse repetition rate of 250 kHz. Field ionized events are recorded on the particle detector and the detector coordinates are accessible through the EPOS file format. Matlab and Python scripts were then used to process the data, scripts which would be made available upon request to the authors.

Results

Pure Metals: Experiments

Analytical FIM combines the imaging capability of FIM with the possibility of detecting the ion following its field evaporation, thereby estimating the difference in the imaging ions and corresponding field evaporated atom directly accessible. An aFIM analysis of a pure W specimen is shown in Figure 2. First, an equivalent FIM image is built by forming a histogram of the imaging gas ion detector hits (Fig. 2a). The typical ring features appear around the main sets of crystallographic planes, as expected. We plot in Figure 2b the location of the W^{3+} and W^{4+} ions that appeared as part of the multiple hits. As expected from the early work of Waugh et al. (1976) comparing FIM and field desorption, the atomic sharpness of the image is lost. The pattern formed is close to the typical desorption pattern observed in APT for higher charges states and multiple hits detected in the analysis of pure W.

We acquired another aFIM dataset on pure W also at 50 K on the LEAP 5000 XS, with a 35% pulse fraction over a standing 6 kV, and 0.15 to 3.6×10^{-8} Torr of He. Filtering techniques for the time-of-flight spectrum in aFIM are described in Katnagallu et al. (2019) and enabled by the correlations in the field evaporation process: the local rearrangements of the charges following the field-induced desorption of an imaging gas atom adsorbed on the surface causes a sudden increase in the local electrostatic field that the neighboring surface atoms are subjected to Katnagallu et al. (2018), which favors their field evaporation in close spatial and temporal correlation (De Geuser et al., 2007).

Figure 3a shows the corresponding mass spectrum from this dataset, with all the data shown in black, and the data following filtering specifically for ions on multiple hits within selected ranges of the mass-to-charge ratio and for impacts that are within 4 mm of each other on the detector. The vast majority of multiple hits processed are Ne–W or He–W (>92.9%), and not just W–W multiple hits. This trend is not surprising considering the higher gas pressure. It is also documented that the probability of multi-hit detection is directly proportional to the strength of the electrostatic field and hence the detection rate (De Geuser et al., 2007). Here, the charge-state ratio of W (taken as the number of W^{3+} ions detected over W^{4+}) in the case of APT (15% PF, 50 K) is 30.44, whereas in the aFIM case (35% PF, 50 K, 10^{-8} Torr of

He), it is only 9.52. This indicates that we are under 5–10% lower electrostatic field conditions according to Kingham's calculations (Kingham, 1982). This was to be expected from Müller's early work on the influence of gas on the field evaporation (Müller et al., 1965).

It is apparent from the filtered mass spectrum, that some Ne remained in the FIM gas mixing chamber. Ne has a lower ionization field than He and cannot be used to image high evaporation field materials like W, as the ionization occurs too far from the specimen's surface to lead to a high-resolution image (Nishikawa & Muller, 1964). Ne can, however, adsorb on the cold specimen's surface and migrate up the shank toward the highest electric field regions. Adsorbates on top of a W atom is expected to strongly attract and localize the charges (Neugebauer & Scheffler, 1993), which can have two consequences. First, upon field desorption of the Ne, the redistribution of these charges will cause the neighboring W atoms underneath to be subject to a higher electrostatic field, thereby enhancing their probability of field evaporation (Katnagallu et al., 2018). Second, both the He or Ne adsorbate and the W atom depart together, possibly aligned along the field line to maximize polarization, and fall apart early during the flight, on the way to the detector, once they have acquired enough charge to be subject to Coulomb explosion (Tsong, 1985; Blum et al., 2016; Zanuttini et al., 2017; Peng et al., 2019). It is worth nothing though that the difference in mass by a factor of 9 and 20 with Ne and He, respectively, makes the trajectory of the W least likely affected by Coulomb repulsion associated with a dissociative event. Either of these mechanisms would result in strong multi-hit correlations (De Geuser et al., 2007; Saxey, 2011; Yao et al., 2013), that is, the detection of a He/Ne ion is often associated with the detection of a W ion from very close locations on the detector.

In Figure 3b, we plotted a detector hit density map using approximately 280 million ion impacts, similar to Figure 2a. Albeit with a slightly coarser binning and with a lower gas pressure that affects the imaging conditions, poles are clearly visible. We superimposed onto this map a quiver plot visualizing the average distance between the impact of a W^{3+} ion and a Ne^+ generated by the same HV pulse over the entire analysis. The corresponding vector is typically oriented radially with respect to the center of the nearest large terrace, pointing inward, that is, the W^{3+} impact is farther from the terrace's center. Figure 3c maps the standard deviation of the displacement between hits that can be up to 0.4 mm. The distance between impacts is low near sets of atomic planes with high-Miller indices, that is, on which the atomic packing is relatively loose and the image resolution in FIM is sufficient to distinguish individual atoms (Chen & Seidman, 1971). The longer distances appear near to the (011) set of planes, that is, the denser planes with the wider spacing and hence the widest terraces that lead to the build-up of stronger electrostatic gradients.

A quantitative analysis of these aberrations is out of the scope of the present article, in part because to be meaningful, this would require a thorough and systematic investigation, but also because the actual magnitude of the aberrations will vary over the course of the analysis as the specimen shape and the magnification evolve and is subject to substantial variations across the field of view as highlighted in Figure 3c. It must also be pointed out that although the charge-state ratio indicates electrostatic fields in the same range, opposite to when laser pulsing is used for instance (Gault et al., 2011a), the presence of the gas can modify the field evaporation conditions, and to quote Erwin Müller: "The
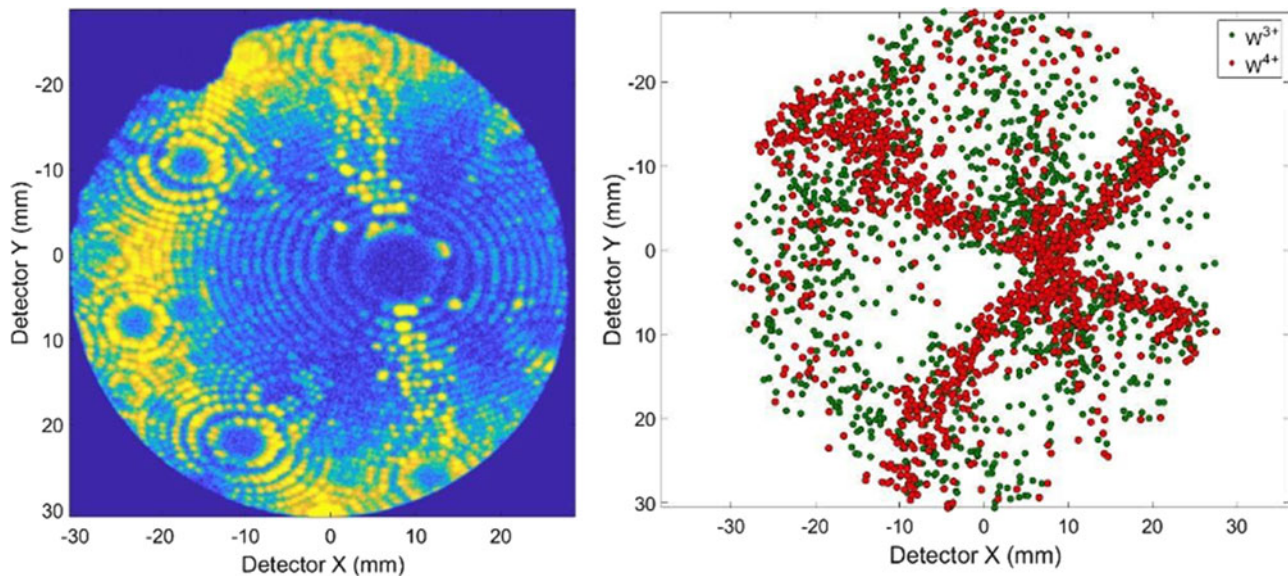
Fig. 2. Image formed from field ionized events on the detector (left) and hit positions of the identified W ions on the detector (right) consistent with field desorption maps seen from APT runs of the higher charge states for pure W.

gas-surface interactions at the emitter tip of a field-ion microscope are quite complicated, and a quantitative understanding is difficult because of the many uncertainty factors of thermal accommodation, particularly in the presence of an adsorbed layer" (Müller et al., 1965).

Pure Metals: Computational Study

As expected from modeling work, the aberrations are intimately linked to the atomic-scale structuring of the specimen's surface, that is, terracing and local neighborhoods. In order to directly compare our experimental observations with simulations, we generated needle-shaped synthetic data for a pure metal with a body-centered crystal structure to mimic W. The specimen's radius was 12 nm. This was used as input for simulating FIM images and APT data.

Figure 3d shows part of a simulated FIM image centered on the (011) terrace in white, with individual atomic positions imaged. A quiver plot is superimposed, with red vectors starting from the location of the impact of the ion following its field evaporation and propagation from the specimen's surface onto the virtual detector and pointing to the corresponding position of the imaged atom in the FIM simulation. A similar set of observations can be made: aberrations are mostly centrifugal with respect to the terraces, and low-index poles lead to more pronounced aberrations. A key message from these results is that the regions primarily badly affected by trajectory aberrations are the low-density areas on the desorption image, which are typically where the atomic planes can be imaged in the depth of the reconstructed dataset in APT (Moody et al., 2009) and FIM (Vurpillot et al., 2007; Klaes et al., 2021). Higher-index poles are, however, expected to exhibit a lower depth resolution (Gault et al., 2009). These simulations point to a necessary compromise between the lateral and depth resolution.

In an effort to quantify the influence of these aberrations on the spatial performance of APT, we performed a series of calculations schematically depicted in Figure 4a. We consider the distance to all atoms in the first shell of nearest-neighbor atoms

sitting on the same plane, which we refer to as D-1NN. These distances are extracted from a Delaunay tessellation (Lefebvre et al., 2011; Felfer et al., 2015) and calculated for all ions in a reconstructed dataset that covers an angular field of view of ±30° around the [011] direction in the center of the virtual detector. The D-1NN in the input simulation cell can be directly compared with the distance to this very same nearest-neighbor in the reconstructed data. We also extract more specifically the offset in depth, dz-1NN. This offset is related to the angular difference in their trajectory, but also to the sequence in which the ions are detected, that is, when two atoms evaporate rapidly after one another, the dz is typically low—see Vurpillot et al. (2013) for more details. Here, we perform this calculation to estimate the spatial dispersion induced by the imaging process for a FIM image simulation for a body-centered cubic crystal, and for atoms on the same (011) atomic plane and for a field of view similar to experimental data.

The histograms of distances to the first nearest-neighbor and z-offset are plotted in Figure 4b. The distribution in the input simulation cell, prior to the imaging and evaporation simulation, is shown in orange. All distances are in a single bin, which reflects the undistorted value in the original bcc crystal. The distribution in the 3D FIM reconstructed volume using the protocol introduced by Klaes et al. (2021) is shown in blue. The distribution is rather narrow around the expected theoretical value, with a full width at half maximum (FWHM) of approximately 0.15 nm, that is, around half of the distance to the first nearest neighbors, making it possible to separate the two neighboring atoms, that is, all atoms are within twice the initial nearest-neighbor distance. The dz-1NN also shows a narrow spread of approximately 0.015 nm FWHM, emphasizing once again the better spatial resolution in depth compared to laterally (Klaes et al., 2021). In the inset is the map representing the pile-up of positions of FIM atomic spot centers obtained after the evaporation of several surface layers. The color scale corresponds to the ion impact density, calculated around each impact using the number of counts in a delimited circle, with a radius equivalent to about 1 nm at the tip surface.
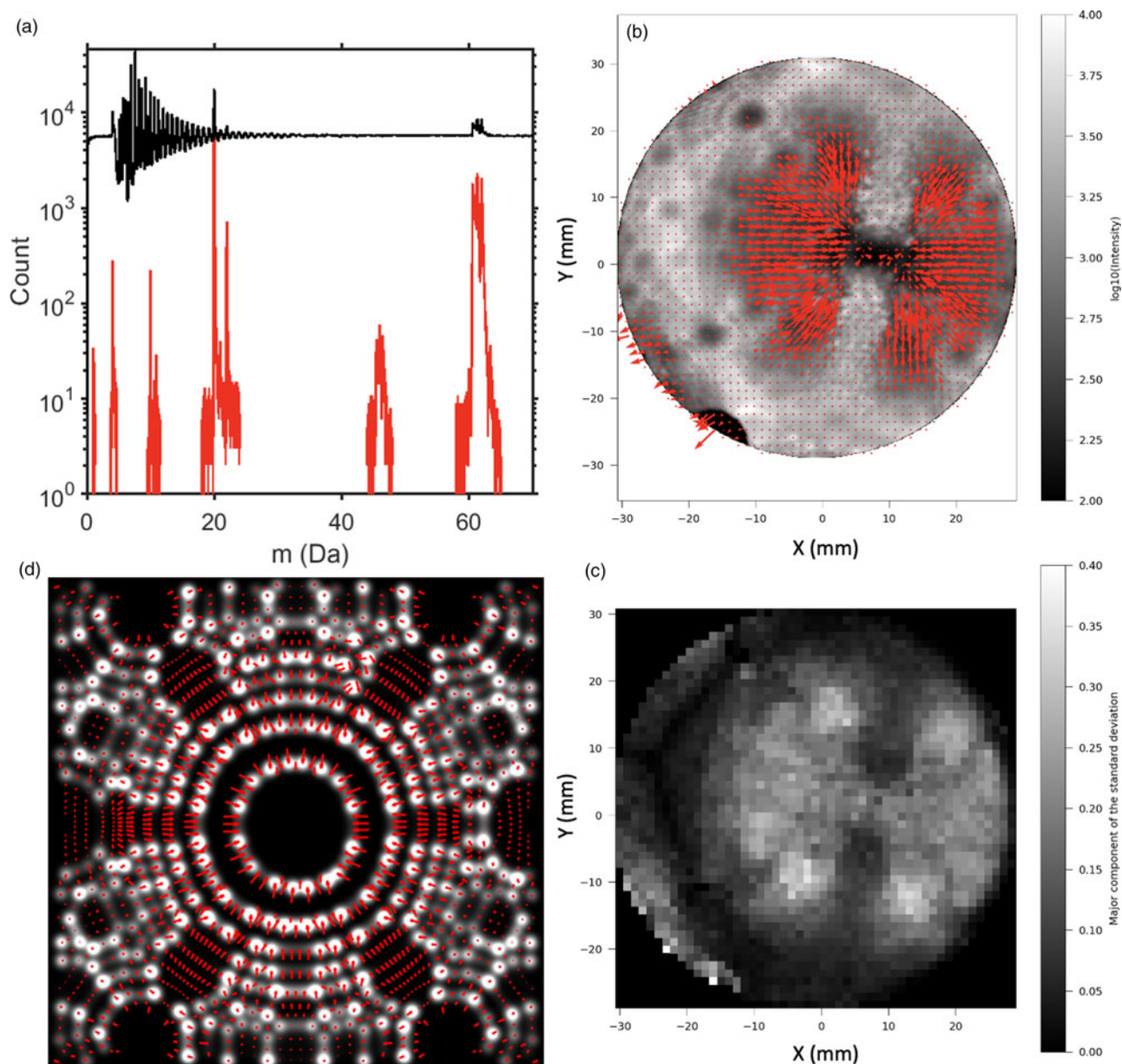
Fig. 3. (**a**) Unfiltered (black) and filtered mass spectra for an aFIM experiment from pure W in He at 50 K. (**b**) Quiver plot of the distance from the impact of a W^{3+} atom to a Ne^+ (approx. 10 million pairs), superimposed on a recalculated equivalent FIM image (280 million hits), and (**c**) map of the standard deviation of the associated displacement. (**d**) FIM image simulation in black and white, and superimposed quiver plot with vectors starting from an ion impact position and pointing to its corresponding location on the FIM image.

Figure 4c shows the same histograms obtained from the corresponding APT simulation, the inset is the detector impact map. The picture here is very different. The FWHM may not have changed much, still near 0.15 nm. However, the peak position has shifted toward a lower distance (0.2 nm instead of 0.22 nm, i.e., approx. 10% difference) from the theoretical value, which indicates significant density fluctuations (Stephenson et al., 2007). More worryingly, nearly 17% of the ions have landed at a distance twice or more than the expected value, making it very unlikely that two neighbors from within the initial volume are indeed neighbors in the reconstructed data. The spread in distances is further evidenced in the graphs shown in a log scale (see Supplementary material).

In Alloys: Simulations

In order to assess these effects in the case of alloys, we revisited the APT simulations performed in the study of a Ni-2% Re alloy by APT and analytical FIM and reported in Katnagallu et al. (2019). In this case, the Re atoms are simulated by a high-field solute segregated to stacking faults formed by deforming pure Ni by molecular dynamics in the large-scale atomic/molecular massively parallel simulator (LAMMPS). 20% of the sites on the stacking faults are replaced by atoms with a 30% higher evaporation field than the matrix. A view of the simulation cell before field evaporation is shown in Figure 5a, with the Ni matrix atoms in green and the high-field Re atoms in purple. Robin-Rolland simulation code was used on a 12 nm radius
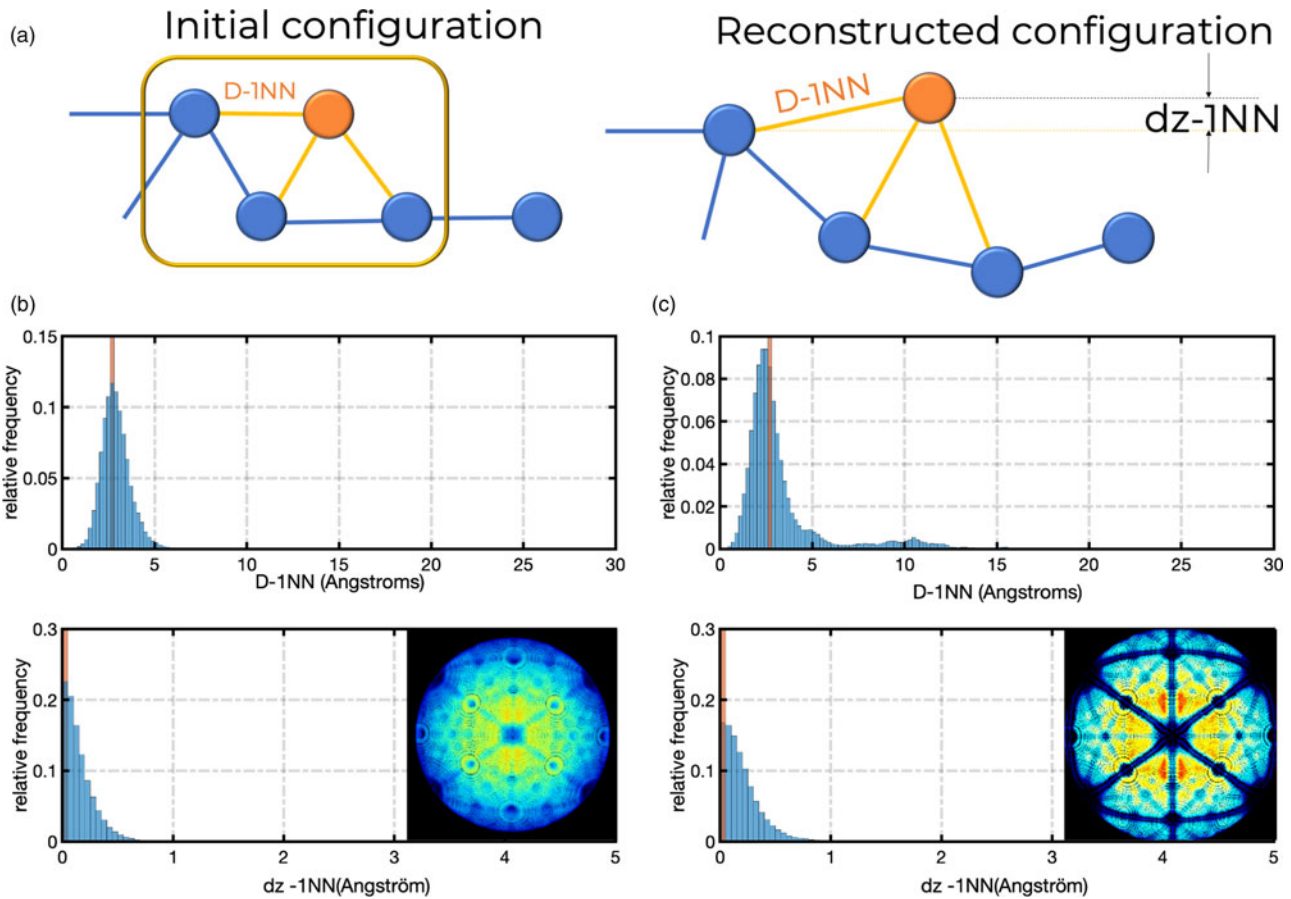
Fig. 4. (**a**) Schematic of the initial and reconstructed atomic configurations, and the calculated quantities: the first near-neighbor distance D-1NN and the z-offset dz-1NN. D1NN and dz-1NN for atoms initially on the same plane in the input data in (**b**) a reconstructed FIM dataset (inset is the multilayer detector map); and (**c**) the corresponding reconstructed APT simulated data. Note that the orange bar in each histogram represents the initial D-1NN and dz-1NN distributions from the same volume of a perfect lattice, whereas the blue histograms represent the measured D-1NN and dz-1NN histograms of distances (using the indexes of the first nearest neighbors) in the reconstructed volumes.

NiRe modeled tip using basic single evaporation field constants for Ni and Re, at $T = 0$ K. Impacts on a detector placed at 1 μm in front of the sample were used to reconstruct a virtual APT volume. As reported in Katnagallu et al. (2019), reconstruction parameters were optimized to have a volume with the correct initial known dimensions. Figure 5b shows a thin slice through the data reconstructed following the simulation of the field evaporation process. The atomic planes are imaged parallel to the tangent to the local reconstructed curved surface across the field of view, that is, (002) planes in the center and the (022) planes toward the edges of the volume.

Figure 5c show the histograms of the nearest-neighbor distance and z-offset, respectively, between a Re atom and its first nearest-neighbor Re atom. In this case, almost half of the Re atoms that were initially first neighbors end up shifted by more than twice the first nearest-neighbor distance. The distribution in the input data, in orange, is not infinitely narrow because of the defects that shift atoms from their ideal positions. The difference with the distribution of the nearest-neighbor distance in the reconstructed data in blue is readily visible: some atoms are reconstructed over a nanometer away from each other, five or more interatomic distances away from where they were initially.

With regards to the z-offset specifically, and conversely to the distributions in Figure 4c, the distribution is substantially distorted. This can be ascribed to a combination of effects. First,

preferential retention of the Re with a higher evaporation field than the Ni matrix modifies the sequence of detection and causes Re atoms to be reconstructed deeper than they should have been. Second, the assumed curvature of the emitter in the reconstruction protocol means that two initially neighboring atoms will be reconstructed at increasingly different depths as their respective impact positions are farther from each other (Gault et al., 2011b).

Concentrated Solid Solutions

Here, we wanted to simulate the case of a high-entropy alloy, which can also be referred to as a compositionally complex alloy or a concentrated multi-component solid solution. These alloys are the focus of many studies at the moment, and one of the most widely studied compositions is an equiatomic mixture of Fe, Cr, Ni, Co, and Mn. These elements are expected to have close evaporation fields in their pure form, nearly all within 25% around 30 V/nm (Tsong, 1978). The evaporation field is species dependent but also depends on the local neighborhood at the specimen's surface (Ge et al., 1999). An approach to model this is to assume a single average evaporation field, modulated randomly to mimic the different species. As input for the simulations, we hence assumed an equiatomic mixture of atoms from five species, randomly distributed on a body-centered cubic lattice. Each species is given a specific evaporation field in the range ±5, ±10, and ±20% around an
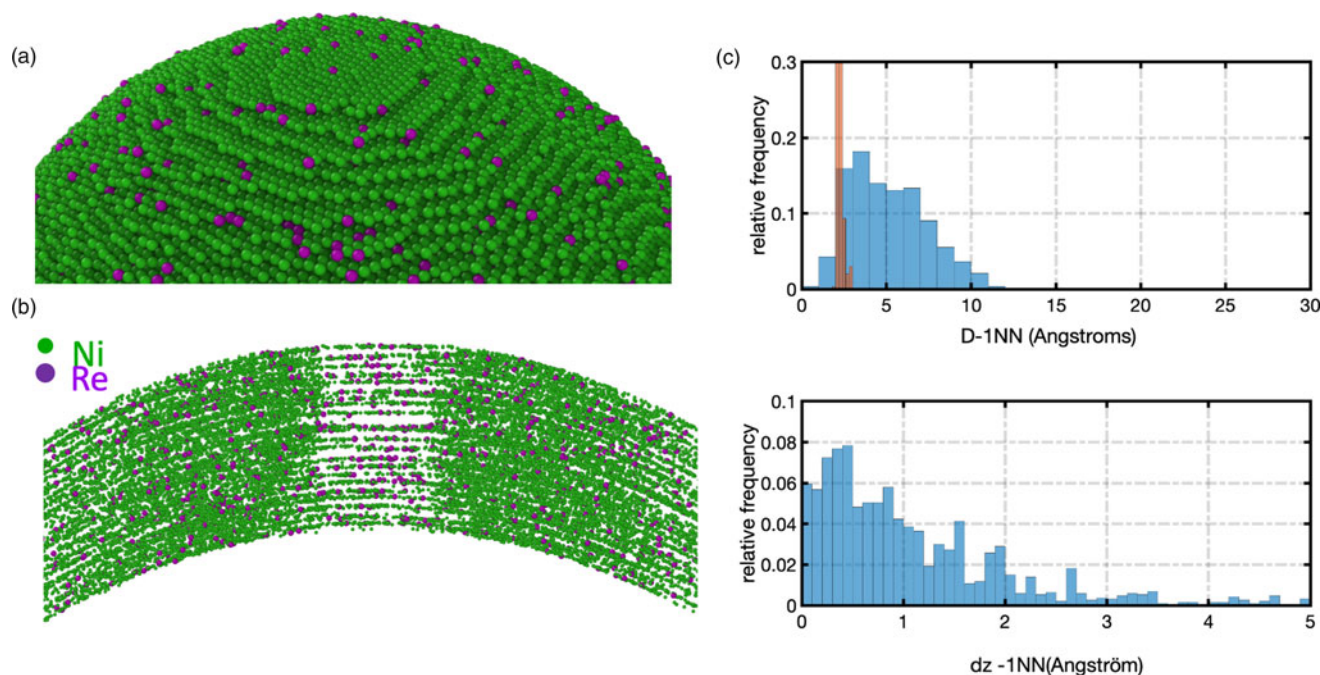
Fig. 5. (**a**) Simulation cell with Re segregated to stacking faults in Ni and (**b**) thin slice though the reconstructed simulated data. (**c**) D-1NN and dz-1NN for Re atoms initially on the same plane in the input data in orange and in the simulated and reconstructed data in blue.

average value. A face-centered cubic lattice would have been closer to most studied alloys, but based on similarities in the aberration patterns from simulations from the different crystal structures (Oberdorfer et al., 2015), we expect that qualitatively similar results would have been obtained. Robin-Rolland simulation code was used on a 25 nm radius modeled tip at $T = 0$ K.

Figure 6 summarizes the results from the simulations for the ±5, ±10, and ±20% ranges, respectively in Figures 6(a)–6(c). The average composition is close to the expected 20% for all elements except in specific regions near poles, where the elements of higher evaporation field are much more highly concentrated—up to approximately 40%. Similar issues had been reported in the past in the analysis of Al alloys for instance (Gault et al., 2012*b*), and it was often thought to be related to surface migration (Gault et al., 2012*a*), which are not accounted for in our model, conversely to others (Gruber et al., 2011), and hence cannot explain these results. This is related to the specific retention on the surface of the field evaporating specimen of the species of highest evaporation field until the local curvature near atoms of that species allows for reaching a sufficient electric field to cause its departure. Since the sequence in which ions are detected is used to derive the *z*-coordinate of each atom during the data reconstruction process, such a retention effect will not only affect the apparent composition but also the depth resolution.

Figure 7 reports the distance and *z*-offset distributions between atoms initially nearest neighbors in the input data for the three ranges of evaporation fields ±5, ±10, and ±20%. The FWHM of the D-1NN distribution changes substantially, increasing from approximately 0.3 nm to 0.75 nm to 1.2 nm, and in depth (*z*-offset) from 0.04 nm to 0.075 nm up to 0.1 nm as the range of evaporation field increases. The precision of the measurement, hence, worsens with the compositional complexity increasing, with a clear mixing of nearest-neighbor positions. The depth coordinate is affected but not as much and the depth resolution is, hence, more robust against the distribution of

evaporation fields within the material, agreeing with experimental observations.

General Discussion

Across the different cases we have studied here, we revisited two important aspects of APT analysis: (1) the spatial resolution is not isotropic, and the depth resolution remains higher than the lateral resolution; and (2) the depth resolution is optimal near the poles, that is in very specific locations within a dataset and not across the entire field-of-view. The depth resolution mostly relates to how sequential the field evaporation proceeds, which can be ascribed to how well the field localizes on the edges of terraces. On dense planes, with a wide interplanar spacing, terraces are wide and the unraveling of the atomic structure by field evaporation follows a well-defined sequence. On open planes, the concentration of the field is less on the edges of the terraces, but on individual atoms. This is what enables true atomic resolution in FIM, but also makes the sequence of evaporation less well determined. This underpins the compromise between lateral and depth resolution that was mentioned above. Evaporation field variations make this balance more difficult to achieve, because they firstly hinder a well-sequenced evaporation, and the atoms with a higher evaporation field remaining on the surface can further cause lateral aberrations. Ultimately, neighborhood analyses should typically be restricted to where atomic planes can be imaged as they are a sign that the field evaporation process is sufficiently well ordered to maintain the neighborhood relationships. However, they can also be locations of aberrant compositional analyses. Let us discuss specific aspects.

Pure Metals

The results we presented herein are not meant to be dismissive of previously published reports in the literature, but merely to get the
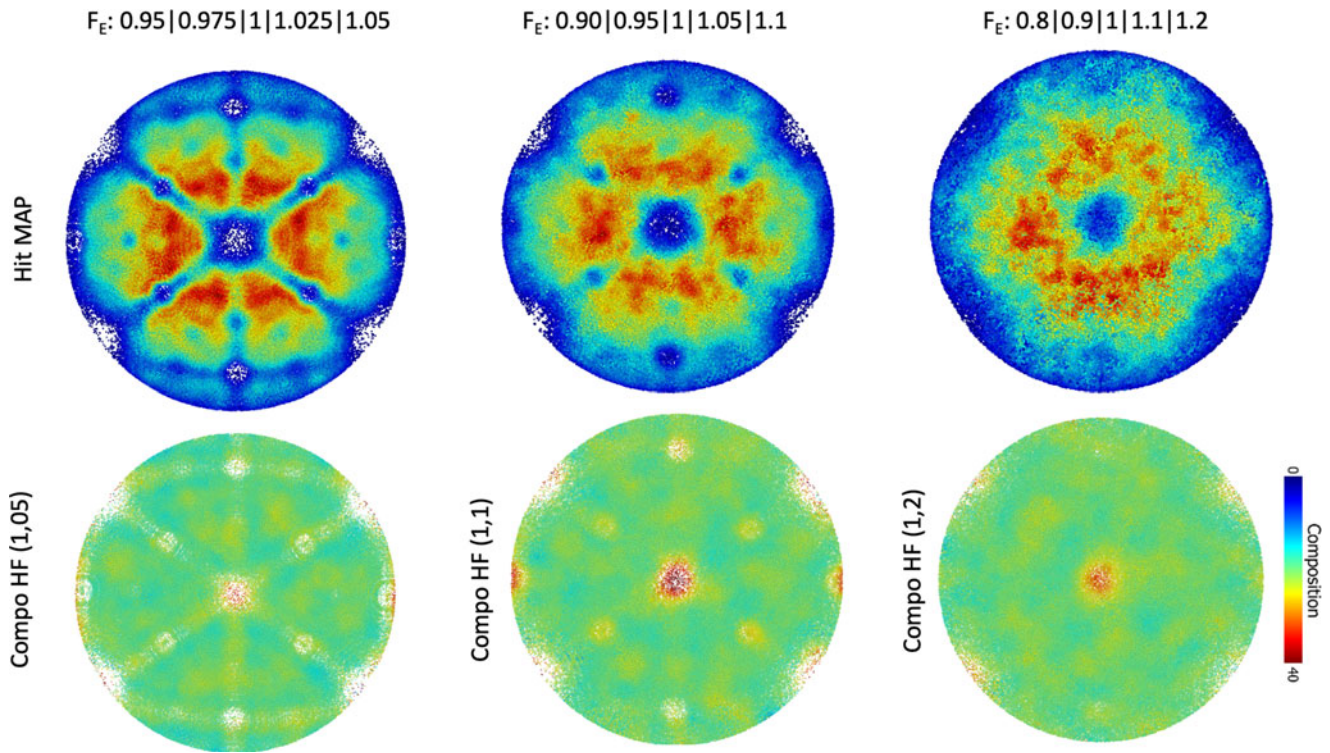
F_E: 0.95|0.975|1|1.025|1.05 F_E: 0.90|0.95|1|1.05|1.1 F_E: 0.8|0.9|1|1.1|1.2

Fig. 6. Overall density map and composition map for the element of highest evaporation field for simulated data with elements with evaporation fields in the range (**a**) 0.95–1.05, (**b**) 0.9–1.1, and (**c**) 0.8–1.2.
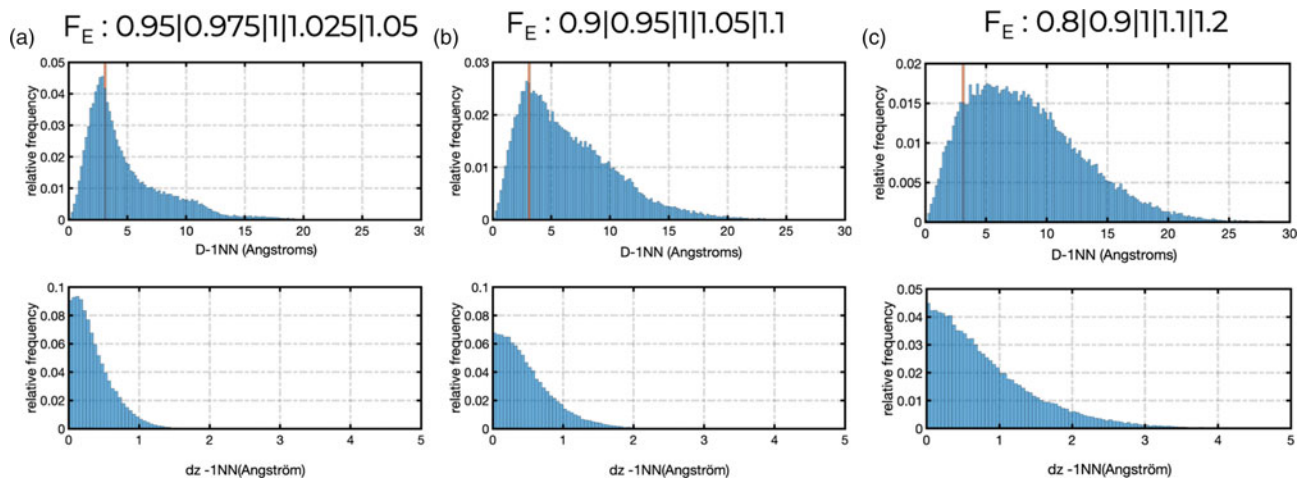

Fig. 7. D-1NN and dz-1NN distributions between atoms initially nearest neighbors and located at the same depth in the input data after field evaporation simulation and data reconstruction for a range of evaporation field of (**a**) ±5%, (**b**) ±10%, and (**c**) ±20% around an average field.

reflection going on what information APT can confidently provide. Some of the authors themselves have reported on the study of atomic neighborhoods (Stephenson et al., 2007) and even on exploiting this information to try and reconstruct lattice positions in pure metals (Vurpillot et al., 2003; Moody et al., 2011; Breen et al., 2015) and alloys (Moody et al., 2014; Gault et al., 2017). A critical perspective should have arisen from the low signal-to-background ratio in the *x-y*-spatial distribution maps from which the lateral resolution of APT was estimated: even in pure metals, with a narrow distribution of evaporation fields (Yao et al., 2015), only a small fraction of neighboring atoms is

reconstructed at distances compatible with their actual first shell of nearest neighbors. This was evident in Moody et al. (2009) and was discussed at length also in other reports (Haley et al., 2009).

Instead, we maintained a misleading impression that despite its apparent limitations, the lateral resolution of APT remained sufficient to resolve the lateral extent of atomic arrangements. Many have heard of projects hoping to achieve full crystallographic analysis from APT data, for instance, Ziletti et al. (2018), especially motivated by the advent of machine-learning and its application in related fields (Butler et al., 2018; Aguiar

et al., 2019). However, the physics governing the early stages of the departure of the charged particle from the surface critically limit the lateral resolution of APT. The probabilistic nature of the process makes it extremely challenging, if possible at all, to correct for the resulting aberrations.

Alloys

First, the set of simulations included herein also shows that detection of high-field species at the center of the poles is not only related to surface diffusion but to the difference in the evaporation field behavior between high field and low field. This affects, for example, AlCu or AlSi and can be ascribed to "chromatic aberrations" as discussed in Marquis & Vurpillot (2008).

Second, our results in the analysis of solutes segregated in a binary alloy point to limitations both in the lateral and depth coordinates. A 30% difference in evaporation field between solutes and solvent is reasonable. Based on tabulated values of the evaporation field, which is admittedly an approximation, this would be less than the difference between Al and Cu for instance, combinations for which the comparison between small-angle scattering data and APT in the analysis of clusters show strong differences (De Geuser & Gault, 2020). Neighborhood relationships in these clusters are hence highly unlikely to be maintained and this raises questions as to the pertinence of nearest-neighbor-based cluster-search algorithms (Dumitraschkewitz et al., 2018). Over the course of a single experiment and across the field of view, the actual distance to a first nearest neighbor can change due to the magnification being non-isotropic and associated with the change in the magnification as the specimen gets blunter due to field evaporation. These aspects make approaches based on radial distribution functions to extract the characteristics of populations of clusters (Zhao et al., 2018) relatively more robust.

Error Estimation

We feel it is pressing that the community comes to terms with these limitations and makes use of the technique for its strengths, without attempting to exploit it for what it is not. This should not prevent us from trying to push the performance limits of APT, and challenge its limitations, but keeping in mind that the limits are mostly bound by the physics and not by the way we extract or process the data. For instance, and despite its inherent limitation, there is still much that APT can do, including in the analysis of crystallographic features patterns (Gault et al., 2012c), by focusing on the analysis of the desorption patterns to work out orientation (Wei et al., 2018) or by using the more highly resolved information in the depth to investigate site occupancy (Li et al., 2021). The difference in the evaporation field between species in a mixture may also preclude some of these analyses.

The depth resolution is relatively robust against changes in the base temperature in high-voltage pulsing mode and peak temperature in laser pulsing mode for pure metals (Gault et al., 2010a, 2010b, 2011a). However, the relative difference in the evaporation field between species can differ as a function of the temperature (Wada, 1984), and, hence, the situation could worsen more substantially in specific cases and lead to a critical loss of resolution that was for instance observed in some ordered phases (Vurpillot et al., 2000b; Boll et al., 2007). Performing these analyses might require careful experimental design, for instance, by preparing specimens along specific orientations as discussed in Jenkins

et al. (2020), optimizing the experimental conditions (pulsing mode, base temperature, detection rate), and targeting the search for short-range ordering in metallic alloys along the direction where the depth resolution is potentially sufficient to reveal the signal—that is, typically low-index sets of planes.

It is also critical that we accept that the precision of our measurement is limited and we should probably get better, as a community, at assessing the spatial error on the atomic positions. For instance, it is commonly accepted that error bars are included in the composition measurement in a composition profile. Even if these errors might be underestimated as they do not account for species-specific losses associated with detector pile-up (Meisenkothen et al., 2015; Peng et al., 2018) or molecular dissociations leading to neutral fragments for instance (Gault et al., 2016; Zanuttini et al., 2017). However, using error bars on the distance axis is most uncommon.

It may be that the representation as a point cloud is misleading—the location at which we reposition a single atom is just one of the possible positions where this atom may have been reconstructed, and it might not be the most probable position where it was located. We do not offer ready-made solutions here, simply point to some of these issues and highlight their complexity, in the hope to raise consciousness and motivate, maybe, studies in this exciting direction.

Conclusion

To conclude, lateral neighborhood relationships within materials are modified and typically not maintained by the field evaporation and APT data reconstruction process. Measured relationships should not be readily interpreted, and only directional neighborhood analyses in the depth may contain relevant information. This was hinted at in previous works, and we provide further evidence here that this affects not only pure metals or metallic glasses, but also when atoms of different evaporation fields are segregated within a matrix, and in compositionally complex alloys. The resolution is more robust in depth, and it is necessary to develop approaches to probe neighborhoods selectively in this direction. This may enable to exploit the higher resolution in this direction to reveal neighborhood relationship, for example, short-range order. Since the aberrations arise in the early stages of the ionic flight, imaging of the atomic neighborhoods prior to the field evaporation, by using field-ion imaging and aFIM in particular, bears a lot of potential for the future.

References

Aguiar JA, Gong ML, Unocic RR, Tasdizen T & Miller BD (2019). Decoding crystallography from high-resolution electron imaging and diffraction data-sets with deep learning. *Sci Adv* **5**, article number, eaaw1949.

Ashton M, Mishra A, Neugebauer J & Freysoldt C (2020). Ab initio description of bond breaking in large electric fields. *Phys Rev Lett* **124**, 176801.

Blavette D, Sarrau JM, Bostel A & Gallot J (1982). Direction and depth of atom probe analysis. *Rev Phys Appl* **17**, 435–440.

Blum I, Rigutti L, Vurpillot F, Vella A, Gaillard A & Deconihout B (2016). Dissociation dynamics of molecular ions in high DC electric field. *J Phys Chem A* **120**, 3654–3662.

Boll T, Al-Kassab T, Yuan Y & Liu ZG (2007). Investigation of the site occupation of atoms in pure and doped TiAl/Ti$_3$Al intermetallic. *Ultramicroscopy* **107**, 796–801.

Breen AJ, Moody MP, Ceguerra AV, Gault B, Araullo-Peters VJ & Ringer SP (2015). Restoring the lattice of Si-based atom probe reconstructions for enhanced information on dopant positioning. *Ultramicroscopy* **159**, 314–323.

Butler KT, Davies DW, Cartwright H, Isayev O & Walsh A (2018). Machine learning for molecular and materials science. *Nature* **559**, 547–555.

Cadel E, Vurpillot F, Larde R, Duguay S & Deconihout B (2009). Depth resolution function of the laser assisted tomographic atom probe in the investigation of semiconductors. *J Appl Phys* **106**, 44908.

Cerezo A, Warren PJ & Smith GDW (1999). Some aspects of image projection in the field-ion microscope. *Ultramicroscopy* **79**, 251–257.

Chen YC & Seidman DN (1971). Atomic resolution of a field ion microscope. *Surf Sci* **26**, 61–84.

De Geuser F & Gault B (2017). Reflections on the projection of ions in atom probe tomography. *Microsc Microanal* **23**, 238–246.

De Geuser F & Gault B (2020). Metrology of small particles and solute clusters by atom probe tomography. *Acta Mater* **188**, 406–415.

De Geuser F, Gault B, Bostel A & Vurpillot F (2007). Correlated field evaporation as seen by atom probe tomography. *Surf Sci* **601**, 536–543.

Deng Y, Tasan CC, Pradeep KG, Springer H, Kostka A & Raabe D (2015). Design of a twinning-induced plasticity high entropy alloy. *Acta Mater* **94**, 124–133.

Detor AJ, Miller MK & Schuh CA (2005). An atom probe tomography study of grain boundary segregation in nanocrystalline Ni-W. In *Materials Research Society Symposium Proceedings*, vol. 903, pp. 1–6.

Dumitraschkewitz P, Gerstl SSA, Stephenson LT, Uggowitzer PJ & Pogatscher S (2018). Clustering in age-hardenable aluminum alloys. *Adv Eng Mater* **20**, 1800255.

Felfer P, Ceguerra AV, Ringer SP & Cairney JM (2015). Detecting and extracting clusters in atom probe data: A simple, automated method using voronoi cells. *Ultramicroscopy* **150**, 30–36.

Galtrey MJ, Oliver RA, Kappers MJ, Humphreys CJ, Stokes DJ, Clifton PH & Cerezo A (2007). Three-dimensional atom probe studies of an In$_x$Ga$_{1-x}$N/GaN multiple quantum well structure: Assessment of possible indium clustering. *Appl Phys Lett* **90**, 61903.

Gault B, Chen YM, Moody MP, Ohkubo T, Hono K & Ringer SP (2011a). Influence of the wavelength on the spatial resolution of pulsed-laser atom probe. *J Appl Phys* **110**, 94901.

Gault B, Cui XY, Moody MP, Ceguerra AV, Breen AJ, Marceau RKW & Ringer SP (2017). A nexus between 3D atomistic data hybrids derived from atom probe microscopy and computational materials science: A new analysis of solute clustering in Al-alloys. *Scr Mater* **131**, 93–97.

Gault B, Danoix F, Hoummada K, Mangelinck D & Leitner H (2012a). Impact of directional walk on atom probe microanalysis. *Ultramicroscopy* **113**, 182–191.

Gault B, Haley D, De Geuser F, Moody MP, Marquis EA, Larson DJ & Geiser BP (2011b). Advances in the reconstruction of atom probe tomography data. *Ultramicroscopy* **111**, 448–457.

Gault B, Moody MP, Cairney JM & Ringer SP (2012b). *Atom Probe Microscopy*. New York, NY: Springer New York.

Gault B, Moody MP, Cairney JM & Ringer SP (2012c). Atom probe crystallography. *Mater Today* **15**, 378–386.

Gault B, Moody MP, De Geuser F, La Fontaine A, Stephenson LT, Haley D & Ringer SP (2010a). Spatial resolution in atom probe tomography. *Microsc Microanal* **16**, 99–110.

Gault B, Moody MPMP, De Geuser F, Haley D, Stephenson LTLT & Ringer SPSP (2009). Origin of the spatial resolution in atom probe microscopy. *Appl Phys Lett* **95**, 34103.

Gault B, Müller M, La Fontaine A, Moody MP, Shariq A, Cerezo A, Ringer SP & Smith GDW (2010b). Influence of surface migration on the spatial resolution of pulsed laser atom probe tomography. *J Appl Phys* **108**, 44904.

Gault B, Saxey DW, Ashton MW, Sinnott SB, Chiaramonti AN, Moody MP & Schreiber DK (2016). Behavior of molecules and molecular ions near a field emitter. *New J Phys* **18**, 33031.

Ge XJ, Chen NX, Zhang WQ & Zhu FW (1999). Selective field evaporation in field-ion microscopy for ordered alloys. *J Appl Phys* **85**, 3488–3493.

Gruber M, Vurpillot F, Bostel A & Deconihout B (2011). A kinetic Monte Carlo approach on the influence of temperature. *Surf Sci* **605**, 2025–2031.

Haley D, Petersen T, Barton G & Ringer SP (2009). Influence of field evaporation on radial distribution functions in atom probe tomography. *Philos Mag* **89**, 925–943.

Hetherington MG, Hyde JM, Miller MK & Smith GDW (1991). Measurement of the amplitude of a spinodal. *Surf Sci* **246**, 304–314.

Hirel P (2015). Atomsk: A tool for manipulating and converting atomic data files. *Comput Phys Commun* **197**, 212–219.

Jenkins BM, Danoix F, Gouné M, Bagot PAJ, Peng Z, Moody MP & Gault B (2020). Reflections on the analysis of interfaces and grain boundaries by atom probe tomography. *Microsc Microanal* **26**, 247–257.

Katnagallu S, Dagan M, Parviainen S, Nematollahi A, Grabowski B, Bagot PAJAJ, Rolland N, Neugebauer J, Raabe D, Vurpillot F, Moody MPP & Gault B (2018). Impact of local electrostatic field rearrangement on field ionization. *J Phys D: Appl Phys* **51**, 105601.

Katnagallu SS, Stephenson LT, Mouton I, Freysoldt C, Subramanyam APA, Jenke J, Ladines ANC, Neumeier S, Hammerschmidt T, Drautz R, Neugebauer J, Vurpillot F, Raabe D & Gault B (2019). Imaging individual solute atoms at crystalline imperfections in metals. *New J Phys* **21**, 123020.

Kingham DR (1982). The post-ionization of field evaporated ions: A theoretical explanation of multiple charge states. *Surf Sci* **116**, 273–301.

Klaes B, Lardé R, Delaroche F, Parviainen S, Rolland N, Katnagallu S, Gault B & Vurpillot F (2021). A model to predict image formation in the three-dimensional field ion microscope. *Comput Phys Commun* **260**, 107317.

Kontis P, Köhler M, Evertz S, Chen Y-TT, Schnabel V, Soler R, Bednarick J, Kirchlechner C, Dehm G, Raabe D, Schneider JMM & Gault B (2018). Nano-laminated thin film metallic glass design for outstanding mechanical properties. *Scr Mater* **155**, 73–77.

Krishnaswamy SV, McLane SB & Müller EW (1975). Aiming performance of the atom probe. *Rev Sci Instrum* **46**, 1237–1240.

Lefebvre W, Philippe T & Vurpillot F (2011). Application of Delaunay tessellation for the characterization of solute-rich clusters in atom probe tomography. *Ultramicroscopy* **111**, 200–206.

Li Y, Zhou X, Colnaghi T, Wei Y, Marek A, Li H, Bauer S, Rampp M & Stephenson LT (2021). Convolutional neural network-assisted recognition of nanoscale L12 ordered structures in face-centred cubic alloys. *npj Comput Mater* **7**, 1–9.

Marquis EA & Vurpillot F (2008). Chromatic aberrations in the field evaporation behavior of small precipitates. *Microsc Microanal* **14**, 561–570.

Meisenkothen F, Steel EB, Prosa TJ, Henry KT & Prakash Kolli R (2015). Effects of detector dead-time on quantitative analyses involving boron and multi-hit detection events in atom probe tomography. *Ultramicroscopy* **159**(Pt 1), 101–111.

Miller MK, Shen TD & Schwarz RB (2003). Atom probe studies of metallic glasses. *J Non-Cryst Solids* **317**, 10–16.

Moody MP, Ceguerra AV, Breen AJ, Cui XY, Gault B, Stephenson LT, Marceau RKW, Powles RC & Ringer SP (2014). Atomically resolved tomography to directly inform simulations for structure-property relationships. *Nat Commun* **5**, 5501.

Moody MP, Gault B, Stephenson LT, Haley D & Ringer SP (2009). Qualification of the tomographic reconstruction in atom probe by advanced spatial distribution map techniques. *Ultramicroscopy* **109**, 815–824.

Moody MP, Gault B, Stephenson LT, Marceau RKW, Powles RC, Ceguerra AV, Breen AJ & Ringer SP (2011). Lattice rectification in atom probe tomography: Toward true three-dimensional atomic microscopy. *Microsc Microanal* **17**, 226–239.

Moody MP, Stephenson LT, Ceguerra AV & Ringer SP (2008). Quantitative binomial distribution analyses of nanoscale like-solute atom clustering and segregation in atom probe tomography data. *Microsc Res Tech* **71**, 542–550.

Müller EW & Bahadur K (1956). Field ionization of gases at a metal surface and the resolution of the field ion microscope. *Phys Rev* **102**, 624–631.

Müller EW, Nakamura S, Nishikawa O & McLane SB (1965). Gas-surface interactions and field-ion microscopy of nonrefractory metals. *J Appl Phys* **36**, 2496–2503.

Neugebauer J & Scheffler M (1993). Theory of adsorption and desorption in high electric-fields. *Surf Sci* **287/288**, 572–576.

Nishikawa O & Muller EW (1964). Operation of the field ion microscope with neon. *J Appl Phys* **35**, 2806–2812.

Oberdorfer C, Eich SM, Lütkemeyer M & Schmitz G (2015). Applications of a versatile modelling approach to 3D atom probe simulations. *Ultramicroscopy* **159**, 184–194.

Panitz JA (1973). The 10 cm atom probe. *Rev Sci Instrum* **44**, 1034.

Peng Z, Vurpillot F, Choi P-P, Li Y, Raabe D & Gault B (2018). On the detection of multiple events in atom probe tomography. *Ultramicroscopy* **189**, 54–60.

Peng Z, Zanuttini D, Gervais B, Jacquet E, Blum I, Choi P-P, Raabe D, Vurpillot F & Gault B (2019). Unraveling the metastability of Cn^{2+} (n=2–4) clusters. *J Phys Chem Lett* **10**, 581–588.

Rao JC, Diao HY, Ocelík V, Vainchtein D, Zhang C, Kuo C, Tang Z, Guo W, Poplawsky JD, Zhou Y, Liaw PK & De Hosson JTM (2017). Secondary phases in $Al_xCoCrFeNi$ high-entropy alloys: An in-situ TEM heating study and thermodynamic appraisal. *Acta Mater* **131**, 206–220.

Rolland N, Vurpillot F, Duguay S & Blavette D (2015). A meshless algorithm to model field evaporation in atom probe tomography. *Microsc Microanal* **21**, 1649–1656.

Sanchez CG, Lozovoi AY & Alavi A (2004). Field-evaporation from first-principles. *Mol Phys* **102**, 1045–1055.

Sarker S, Isheim D, King G, An Q, Chandra D, Morozov SI, Page K, Wermer JN, Seidman DN & Dolan M (2018). Icosahedra clustering and short range order in Ni-Nb-Zr amorphous membranes. *Sci Rep* **8**, 6084.

Saxey DW (2011). Correlated ion analysis and the interpretation of atom probe mass spectra. *Ultramicroscopy* **111**, 473–479.

Schmidt WA, Ernst N & Suchorski Y (1993). Local electric-fields at individual atomic surface sites - Field-ion appearance energy measurements. *Appl Surf Sci* **67**, 101–110.

Shariq A, Al-Kassab T, Kirchheim R & Schwarz RB (2007). Exploring the next neighbourhood relationship in amorphous alloys utilizing atom probe tomography. *Ultramicroscopy* **107**, 773–780.

Smith R & Walls JM (1978). Ion trajectories in field-ion microscope. *J Phys D Appl Phys* **11**, 409–419.

Stephenson LT, Moody MP, Liddicoat PV & Ringer SP (2007). New techniques for the analysis of fine-scaled clustering phenomena within atom probe tomography (APT) data. *Microsc Microanal* **13**, 448–463.

Stukowski A (2010). Visualization and analysis of atomistic simulation data with OVITO – the Open Visualization Tool. *Model Simul Mater Sci Eng* **18**, 015012.

Suchorski Y, Medvedev VK & Block JH (1996). Noble-gas-like mechanism of localized field ionization of nitrogen as detected by field ion appearance energy spectroscopy. *Appl Surf Sci* **94–95**, 217–223.

Tsong TT (1978). Field-ion image-formation. *Surf Sci* **70**, 211–233.

Tsong TT (1985). Orientational and isotope effects in field dissociation by atomic tunneling of compound ions. *Phys Rev Lett* **55**, 2826.

Vurpillot F, Bostel A & Blavette D (2000*a*). Trajectory overlaps and local magnification in three-dimensional atom probe. *Appl Phys Lett* **76**, 3127–3129.

Vurpillot F, Bostel A, Cadel E & Blavette D (2000*b*). The spatial resolution of 3D atom probe in the investigation of single-phase materials. *Ultramicroscopy* **84**, 213–224.

Vurpillot F, Da Costa G, Menand A & Blavette D (2001). Structural analyses in three-dimensional atom probe: A Fourier approach. *J Microsc* **203**, 295–302.

Vurpillot F, Danoix F, Gilbert M, Koelling S, Dagan M & Seidman DN (2017). True atomic-scale imaging in three dimensions: A review of the rebirth of field-Ion microscopy. *Microsc Microanal* **23**, 210–220.

Vurpillot F, Gault B, Geiser BP & Larson DJ (2013). Reconstructing atom probe data: A review. *Ultramicroscopy* **132**, 19–30.

Vurpillot F, Gilbert M & Deconihout B (2007). Towards the three-dimensional field ion microscope. *Surf Interface Anal* **39**, 273–277.

Vurpillot F & Oberdorfer C (2015). Modeling atom probe tomography: A review. *Ultramicroscopy* **159**, 202–216.

Vurpillot F, Renaud L & Blavette D (2003). A new step towards the lattice reconstruction in 3DAP. *Ultramicroscopy* **95**, 223–229.

Wada M (1984). On the thermally activated field evaporation of surface atoms. *Surf Sci* **145**, 451–465.

Waugh AR, Boyes ED & Southon MJ (1976). Investigations of field evaporation with field desorption microscope. *Surf Sci* **61**, 109–142.

Wei Y, Gault B, Varanasi RS, Raabe D, Herbig M & Breen AJAJ (2018). Machine-learning-based atom probe crystallographic analysis. *Ultramicroscopy* **194**, 15–24.

Wilkes TJ, Smith GDW & Smith DA (1974). On the quantitative analysis of field ion micrographs. *Metallography* **7**, 403–430.

Yao L, Cairney JM, Gault B, Zhu C & Ringer SP (2013). Correlating spatial, temporal and chemical information in atom probe data: New insights from multiple evaporation in microalloyed steels. *Philos Mag Lett* **93**, 299–306.

Yao L, Withrow T, Restrepo OD, Windl W & Marquis EA (2015). Effects of the local structure dependence of evaporation fields on field evaporation behavior. *Appl Phys Lett* **107**, 241602.

Zanuttini D, Blum I, Rigutti L, Vurpillot F, Douady J, Jacquet E, Anglade P-M & Gervais B (2017). Simulation of field-induced molecular dissociation in atom-probe tomography: Identification of a neutral emission channel. *Phys Rev A* **95**, 61401.

Zhao H, Gault B, Ponge D, Raabe D & De Geuser F (2018). Parameter free quantitative analysis of atom probe data by correlation functions: Application to the precipitation in Al-Zn-Mg-Cu. *Scr Mater* **154**, 106–110.

Ziletti A, Kumar D, Scheffler M & Ghiringhelli LM (2018). Insightful classification of crystal structures using deep learning. *Nat Commun* **9**, 1–10.